An integrated approach to the key parameters in methanol-to-olefins reaction catalyzed by MFI/MEL zeolite materials

Liu, Chuncheng; Uslamin, Evgeny A.; van Vreeswijk, Sophie H.; Yarulina, Irina; Ganapathy, Swapna; Weckhuysen, Bert M.; Kapteijn, Freek; Pidko, Evgeny A.

DOI
10.1016/S1872-2067(21)63990-6

Publication date
2022

Document Version
Final published version

Published in
Chinese Journal of Catalysis

Chinese Journal of Catalysis 43 (2022) 1879–1893

available at www.sciencedirect.com

ScienceDirect

journal homepage: www.sciencedirect.com/journal/chinese-journal-of-catalysis

Article

An integrated approach to the key parameters in methanol-to-olefins reaction catalyzed by MFI/MEL zeolite materials

Chuncheng Liu [a,d], Evgeny A. Uslamin [a], Sophie H. van Vreeswijk [c], Irina Yarulina [b], Swapna Ganapathy [c], Bert M. Weckhuysen [c], Freek Kapteijn [d,*], Evgeny A. Pidko [a,#]

[a] *Inorganic Systems Engineering, Department of Chemical Engineering, Delft University of Technology, Van der Maasweg 9, 2629 HZ Delft, the Netherlands*

[b] *BASF SE, Process Research and Chemical Engineering, Ludwigshafen 67056, Germany*

[c] *Inorganic Chemistry and Catalysis, Debye Institute for Nanomaterials Science, Utrecht University, Universiteitsweg 99, 3854 CG Utrecht, the Netherlands*

[d] *Catalysis Engineering, Department of Chemical Engineering, Delft University of Technology, Van der Maasweg 9, 2629 HZ Delft, the Netherlands*

ARTICLE INFO

Article history:
Received 8 November 2021
Accepted 4 December 2021
Available online 20 May 2022

Keywords:
Structure-performance relationship
Zeolite catalysis
Methanol-to-olefin conversion
Al-distribution
Acidity
Intergrowth MFI/MEL
Pentasil

ABSTRACT

Identification of the catalyst characteristics correlating with the key performance parameters including selectivity and stability is key to the rational catalyst design. Herein we focused on the identification of property-performance relationships in the methanol-to-olefin (MTO) process by studying in detail the catalytic behaviour of MFI, MEL and their respective intergrowth zeolites. The detailed material characterization reveals that both the high production of propylene and butylenes and the large MeOH conversion capacity correlate with the enrichment of lattice Al sites in the channels of the pentasil structure as identified by ^{27}Al MAS NMR and 3-methylpentane cracking results. The lack of correlation between MTO performance and other catalyst characteristics, such as crystal size, presence of external Brønsted acid sites and Al pairing suggests their less pronounced role in defining the propylene selectivity. Our analysis reveals that catalyst deactivation is rather complex and is strongly affected by the enrichment of lattice Al in the intersections, the overall Al-content, and crystal size. The intergrowth of MFI and MEL phases accelerates the catalyst deactivation rate.

1. Introduction

The methanol-to-olefins (MTO) technology has the potential to play a major role in the sustainable production of light olefins. It is recognized as one of the key ingredients within the methanol (MeOH) economy concept [1,2] enabling the production of the crucial hydrocarbon building blocks, such as light olefins, starting from CO_2 as the primary carbon source [3]. Despite the worldwide industrialization of the MTO process [4–6], intense research is still focusing on a better understanding of the underlying structure-performance relationship for the optimization of this catalytic process and the development of more selective and stable catalytic materials [7–14]. In particular, the growing demand for renewable propylene empha-

* Corresponding author. E-mail: F.Kapteijn@tudelft.nl
# Corresponding author. E-mail: e.a.pidko@tudelft.nl
This work was supported by the BASF and the Advanced Research Center Chemical Building Blocks Consortium (ARC CBBC) for Funding under Project (2016.007.TUD).
DOI: 10.1016/S1872-2067(21)63990-6 | http://www.sciencedirect.com/journal/chinese-journal-of-catalysis | Chin. J. Catal., Vol. 43, No. 7, July 2022

sizes the importance of further optimization of the selectivity of the MTO catalysts towards propylene production.

The mechanism of the MTO process is highly complex. A multitude of parallel and consecutive chemical transformations of the substrates are catalyzed by Brønsted acid sites (BAS) resulting in a range of hydrocarbon products [15–19]. After a rather short induction period, two catalytic cycles involving the interconversion of confined olefinic and aromatic intermediates promote simultaneously the MeOH conversion and the formation of longer-chain hydrocarbons [20–23]. The cracking of the olefinic intermediates in the so-called olefinic cycle is solely responsible for the formation of all olefinic products, with ethylene as exception which is also mainly produced *via* the dealkylation of larger aromatic intermediates within the aromatic cycle [7,24].

The concentration, location, and distribution of BAS are of primary importance to define the activity in the MTO process. By increasing the Al concentration, the chance of interaction between guest substrates and BAS simultaneously increases, eventually promoting the aromatic cycle, increasing aromatics and ethylene formation [25,26]. Zeolites with the same BAS density can also exhibit a substantially different MTO performance, ascribed to the heterogeneous distribution of Al within the crystal [16]. The presence of strong BAS on the external surface of zeolite crystallites was shown to promote coking and decreases the catalyst lifetime [27]. At high Al content when Al ions are in close vicinity, separated by two or more silicon tetrahedra, the so-called Al_{pair} is formed. The cooperation of the BAS associated with such Al_{pair} decreases the energy barrier for the formation of aromatic intermediates [28] eventually increasing the selectivity towards aromatic products at the expense of the selectivity towards propylene.

The relative rates of the two catalytic cycles also depend on the topological properties of the confined space, where the reaction takes place, and they determine the selectivity of the catalytic process. The uniform micropores of the zeolite catalyst ensure the efficient confinement and stabilization of the reaction intermediates (transition-state selectivity [29]), while the pore diameter only allows the products that fit to pass through and escape the zeolite (product-selectivity [29,30]). Among more than 230 zeolite topologies, the 10-membered ring (10-MR) zeolites have attracted great interest in the MTO process [31–35]. Particularly, 10-MR TON-type zeolites consisting of 1-dimensional channels exhibit high selectivity towards C_{5+} hydrocarbons with a negligible contribution of aromatics. Because of shape-selectivity the narrow channels (4.6 Å × 5.7 Å) host the key intermediates of the olefinic cycle, *e.g.* methylcyclopentenyl cations [35,36]. However, the application of TON-type zeolites in the MTO process is hindered by fast deactivation, which is probably due to the rapid coke deposition easily blocking the 1D channels [32,34,35]. In this study, catalysts with zeolite topologies MFI (HZSM-5) and MEL (HZSM-11) of the pentasil family are investigated. These 10-MR zeolite topologies display 3-dimensional channel and intersection systems with very similar diameters. While MFI-type zeolite consists of straight (4.5 Å) and sinusoidal (4.7 Å) channels with intersection (6.4 Å), MEL-type consists of only straight channels (5.2 Å) with intersection (7.7 Å) [37]. These single topologies are further compared with mixed-topology zeolite catalysts consisting of intergrown MFI and MEL crystal phases, indicated by HZBM-10. A detailed skeletal description of how MFI and MEL phases mix at an atomic scale is given in [38]. These 10-membered ring zeolites with 3-dimensional pores have been widely investigated because of the promising selectivity towards propylene and butylenes in MTO combined with the prolonged lifetime in comparison with 1-dimensional 10-MR zeolites [31–33].

The comparative MTO study of MFI-type, MEL-type and TON-type zeolites by Hunger and co-workers [31] showed that under optimized conditions a comparable selectivity towards propylene (~50%) for MFI-type and MEL-type zeolites can be achieved at an optimal BAS density (~15 mmol/g), while the selectivity towards propylene is reduced to ~38% for TON-type zeolites (BAS ~30 mmol/g). The major conclusion was drawn that the BAS density is an important optimizing parameter for tuning the MTO selectivity, but did not provide insight in the relation with the structural properties of those zeolites. Fan and co-workers compared the MTO performance for MFI- and MEL-type zeolite catalyst and demonstrated that the MEL-type H-ZSM-11 is more selective to produce light olefins [33]. Furthermore, it was proposed that for the zeolites with a higher Si/Al ratio (>120), the lattice Al enrichment in the zeolite channels is the key factor that determines the MTO product selectivity. The use of materials featuring an intergrowth framework with mixing MFI and MEL topologies as an MTO catalyst was also shown to enhance the propylene selectivity in comparison with the pure MFI-based HZSM-5 catalysts [39]. By varying the composition of MFI or MEL phases in the zeolite, the MeOH selectivity to propylene could be increased to ca. 46% from 27% for MFI. There is a general consensus in the research community that shape selectivity, ascribed to the subtle differences in the geometry and structure of the zeolite confined space, is one of the key factors that determines the MTO catalyst performance and, particularly, the selectivity towards propylene [40]. However, the different synthesis methods for different zeolite topologies and various post-synthesis approaches inevitably introduced the variation in other parameters including crystal morphology, Si/Al ratio, Al distribution (at internal or external surface, in channels or intersections), and potentially other physicochemical properties, which all may also substantially affect the catalyst behavior. Therefore, an integrated approach for analysing all these parameters is crucial to find out the key parameter(s) to control the catalytic performance. A thorough analysis of the possible correspondence thereafter will lead to a comprehensive structural-performance relationship.

In this study a systematic analysis of all the above-mentioned aspects is performed in an attempt to identify in a comprehensive approach the key descriptors that intrinsically control the MTO performance of the 10-MR zeolites under study, namely HZSM-5, HZSM-11 and an intergrowth phase HZBM-10. With this in mind, steady-state MTO tests combined with *operando* UV-vis spectroscopy measurements firstly emphasized the different catalytic behaviors with respect to selec-

tivity, MTO stability, and various features on the surface of MEL-type, MFI-type, and the intergrowth zeolites. Through a wide range of characterization, spectroscopic measurements, and probe reactions, substantial differences were highlighted on the crystal size, BAS distribution over the crystal, Al_{pair}, and Al-siting of all tested zeolites. Combined with the MTO selectivity and stability, the correlation between each of the parameters and the catalytic performance was thoroughly evaluated and discussed. The significance of each parameter on the product selectivity and lifetime was eventually addressed.

2. Experimental

2.1. Chemicals

All reagents were of reagent grade and used without further purifications: sodium nitrate ($NaNO_3$, Sigma Aldrich, ACS reagent, ≥99.0%), cobalt(II) nitrate hexahydrate (Alfa Aesar, ACS reagent, 98.0%–102.0%), 1,3,5-triisopropylbenzene (1,3,5-TIPB, Sigma Aldrich, 95%), 3-methylpentane (3-MP, Alfa Aesar, 99+%), *n*-hexane (Sigma-Aldrich, 99%), 2,4-dimethylquinoline (2,4-DMQ, Alfa Aesar, 95%), methanol (MeOH, Sigma-Aldrich, for HPLC, ≥99.9%) and deionized water.

2.2. Zeolite materials

Zeolite samples with different topologies including MFI (ZSM-5), MEL (ZSM-11), and intergrowth MFI/MEL (ZBM-10) were obtained from commercial sources. ZSM-5 samples with different Si/Al ratio and crystal size including CBV5020E (Zeolyst Int., Si/Al = 25), BASF1 (BASF, Si/Al = 25) and BASF2 (BASF, Si/Al = 50) are denoted by MFI-25-M, MFI-25-S and MFI-50-S, respectively (S and M indicate the respective small and medium crystal size based on scanning electron microscope (SEM) and X-ray powder diffraction (XRD) analysis). ZSM-11 samples were purchased from ACS Material (MZ110012, Si/Al = 25) denoted as MEL-25-S. Two intergrowth zeolite samples ZBM-10 featuring different crystal sizes were provided by BASF and named as MFI/MEL-25-S and MFI/MEL-50-L, where S and L represent samples with respective small and large crystal size. All the above-mentioned zeolite samples were calcined in air at 550 °C (2 °C/min) for 6 h to obtain the protonic form.

2.3. Chemical composition, structural and textural properties

The chemical composition of zeolite materials was assessed with ICP-AES (inductively coupled plasma atomic emission spectroscopy) using a Perkin Elmer Optima 5300DV instrument (glass torch + saffire injector). Prior to measurement, 50 mg zeolite sample was digested in 4.5 mL 30% HCl + 1.5 mL 65% HNO_3 + 0.2 mL 40% HF using microwave heating for ca. 60 min. The resulting solutions were then diluted to 50 mL with deionized water.

XRD was performed in Bragg-Brentano geometry with a Bruker D8 Advance X-ray diffractometer using monochromatic Co K_α (λ = 1.788970 Å) radiation between 2θ = 5° and 55°. The refinement and quantitative phase analysis were carried out using Topas software. The crystal size analysis was carried out by applying the Scherrer method:

$$D = K \times \lambda/(B \times \cos\theta)$$

where D represents the diameter of a spherical nanocrystal with K = 0.89, λ is the wavelength of X-ray, θ is the diffraction angle of the band at 9.2°, and B is the corrected half width of the observed half width considering the instrumental impact.

Microporous properties of each sample were assessed from N_2 physisorption isotherms at –196 °C using Tristar II 3020. Prior to the measurements, samples were dried and degassed at 350 °C for 6 h under constant N_2 flow.

X-ray Photoelectron Spectroscopy (XPS) was employed to determine the Si/Al ratio on the outer surface of the tested zeolites. XPS spectra were collected using a Thermo Scientific K-alpha spectrometer equipped with a monochromatic Al K_α X-ray source and a 180° double-focusing hemispherical analyser with a 128-channel detector.

2.4. Acid site density and Al distribution

2.4.1. FTIR pyridine adsorption

Transmission FT-IR spectroscopy of adsorbed pyridine as a probe molecule was used to quantify the acid site density of the catalytic materials (MFI-25-S as reference estimated from formula: $H_nAl_nSi_{96-n}O_{192}\cdot 16H_2O$, n = 3.7). Samples (20 mg) were pressed in self-supported wafers with diameter 1.6 cm and then placed in an IR quartz cell. The spectra were collected at 2 cm^{-1} resolution using a Nicolet Nexus spectrometer equipped with an extended KBr beam splitting and an MCT detector. The amount of BAS and LAS was derived from the absorbance at 1545 and 1456 cm^{-1} using the integrated molar extinction coefficients of 0.73 and 1.11, respectively [41]. Assuming that one pyridine molecule is only adsorbed on one BAS/LAS, the following equations were used to estimate C_{BAS} and C_{LAS}:

$$C_{BAS} = 4.30 \times IA(BAS)R^2/W$$

$$C_{LAS} = 2.83 \times IA(LAS)R^2/W$$

where IA (BAS, LAS) represents the integrated absorbance of the band at 1545 and 1456 cm^{-1}, R is the radius of sample wafer (cm) and W is the weight of sample wafer (g).

2.4.2. FTIR of adsorbed CO

To compare the strength of these acid sites, transmission FT-IR spectra with CO as probe was carried out at –140 °C. 10 mg powder was pressed in a self-supported wafer with diameter 0.8 cm. After pre-treating at 400 °C overnight under vacuum, IR spectra were collected at 2 cm^{-1} resolution using a Nicolet Nexus spectrometer within 400–4000 cm^{-1}. During spectra collection, liquid nitrogen is used to maintain the IR cell temperature at ca. –140 °C. The partial pressure of CO was stepwise increased (0.1 mbar per step) through a manifold connected to the specimen holder.

2.4.3. Solid state magic angle spinning (MAS) NMR measurements

MAS NMR measurements of fully hydrated samples were performed on a Bruker Ascend 500 magnet (11.7 T) equipped

with a NEO console operating at a ^{27}Al resonance frequency of 130.32 MHz, using a Bruker 3.2 mm two channel MAS probe head. The MAS rate was set to 20 kHz for all measurements. To obtain the high-resolution ^{27}Al MAS NMR spectrum for quantitative analysis of Al distribution, the single pulse ^{27}Al MAS NMR measurements were recorded with a pulse length of 1.25 μs, a recycle delay of 0.5 s, and 10240 scans each [42]. Two-dimensional (2D) multiple quantum magic-angle spinning (MQ MAS) NMR spectra were measured using a triple quantum z-filter pulse sequence. Excitation and conversion pulses of 3.4 and 1.1 μs and a selective soft pulse of 11 μs for the z-filter filtering were utilized. All 2D spectra consist of 100 transients, each transient incremented by 70 μs with a recycle delay of 0.2 s. Five characteristic peaks with fixed width at 58, 56, 55, 53, and 52 ppm were used for 1D ^{27}Al MAS NMR spectra deconvolution using Voigt function [43,44] (G/L = 0.5 [45]) [33,42,46].

2.4.4. Co(II) ion exchange and UV-vis diffuse reflectance spectra measurements

To analyze the distribution of Al atoms (including Al_{pair} and Al_{single}) locations in the zeolite framework, UV-vis diffuse reflectance spectra (UV-vis-DRS) of fully Co-exchanged zeolites were measured on a Perkin-Elmer Lambda 900 spectrophotometer equipped with an integrating sphere ("Labsphere") using $BaSO_4$ as a reference. Before measurement, the protonic zeolites were exchanged 3 times with 200 mL of 1 mol/L $NaNO_3$ solution per 1 g zeolite at 70 °C. After recovering by centrifugation, Co ion exchange was then performed with 100 mL 0.05 mol/L $Co(NO_3)_2$ solution per 1 g zeolite at room temperature under stirring for 24 h. The exchange was repeated three times with centrifugation between each repetition [47]. Washed by deionized water after the third ion exchange, the obtained Co(II)-exchanged samples were then dried at room temperature under dynamic vacuum and then dehydrated at 400 °C under constant N_2 flow for 7 h before being transferred to the self-sealing UV-vis sample holder in a moisture-free glovebox [48–50]. The absorption intensity is expressed by the Schuster-Kubelka-Munk equation:

$$F(R_\infty) = (1-R_\infty)^2/2R_\infty$$

The distribution of Al atoms in the zeolite framework is categorized as Al_{pair} and Al_{single} as reported by Dedecek *et al.* [47] Co(II) cations are selectively exchanged on Al_{pair} sites under the above-mentioned conditions [51]. Combined with the amount of Na ions remaining in the framework after Co(II) ion exchange, the number of Al_{pair} and Al_{single} can be calculated as below:

$$Al_{single} = [Na]$$
$$Al_{pair} = 2 \times [Co]$$
$$Al_{framework} = [Na] + 2 \times [Co]$$

where [Co] and [Na] represent concentrations of Co^{2+} and Na^+ in the sample determined by ICP-AES after Co ion exchange.

2.4.5. Cracking of 1,3,5-triisopropylbenzene (1,3,5-TIPB)

To probe the external BAS, cracking of 1,3,5-TIPB was used as a probe reaction [52,53]. The catalytic tests were conducted in a fixed bed reactor. 20 mg catalyst (150–212 μm) was activated at 550 °C in 50 mL/min air before reaction at 200 °C. 1,3,5-TIPB in low concentration (0.3% *v*/*v*) was fed with 50 mL/min N_2 after passing through a saturator at 10 °C.

2.4.6. Cracking of 3-methylpentane (3-MP) and n-hexane

To probe the Al-arrangement (channel versus intersection) in the zeolite framework [33,42], the cracking of 3-MP was used as a probe reaction conducted in a fixed bed reactor [54]. In a typical experiment, 20 mg catalyst (150–212 μm) was activated at 550 °C in 50 mL/min air prior to reaction at 400 °C. 2,4-Dimethyl quinoline (2,4-DMQ) base was added to deactivate surface sites [52]. To control total conversion below 10%, the partial pressure of 3-MP was adjusted at 3.8 kPa by passing 50 mL/min N_2 as carrier gas through a saturator at 5 °C. Hydrogen, methane and ethane are selectively formed through the monomolecular cracking of the pentacoordinated carbonium ion formed by the protonation of the 3-MP molecule on the BAS inside the zeolite crystals. In contrast, the energetically favourable bimolecular cracking [55] *via* primary carbenium ions would require a more spacious space to hold the bulkier transition state of 3-MP and forms mainly only hydrocarbons beyond C3. A previous study found that the bimolecular cracking can hardly occur on H-ZSM-22, which displays the 1-dimensional straight 10-MR channels without intersections [42]. Thus, the selectivity towards the cracking products hydrogen, methane and ethane (moles/100 mol cracked) is a good indicator of monomolecular cracking of 3-MP solely on BAS located in the straight or sinusoidal channels.

$$S_{H_2+CH_4+C_2H_6} = (\phi_{CH_4} + \phi_{C_2H_6} + \phi_{H_2})/(\phi_{3\text{-}MP_{in}} - \phi_{3\text{-}MP_{out}}) \times 100\%$$

where ϕ_{Cn} and S represents the molar flow rate and selectivity in unit of moles per 100 mol 3-MP cracked, respectively.

Constraint index (CI) is used to evaluate the steric hindrance of a zeolite topology upon the reactant and represents the ratio of the (assumed) first order rate constants of *n*-hexane and 3-MP cracking [56]. To measure CI for studied materials, a 4 mm (ID) quartz tube reactor was filled with 20 mg sieved zeolite fraction (particle size 150–212 μm). *n*-Hexane and 3-MP were simultaneously fed into the reactor using 10 mL/min He as carrier passing through a saturator containing a mixture of *n*-hexane and 3-MP at 11 °C. The reaction was performed at 400 °C in the presence of 2,4-DMQ to deactivate surface sites [52]. The CI value is calculated as:

$$CI = k_{n\text{-}kexane}/k_{3\text{-}MP} = \ln(1 - X_{n\text{-}kexane})/\ln(1 - X_{3\text{-}MP})$$

2.5. Catalytic performance testing

MTO reactions were performed at 450 °C using a fixed-bed reactor setup. A 4 mm (ID) quartz tube reactor was filled with 40 mg sieved zeolite fraction (particle size 150–212 μm). MeOH was fed into the reactor using a thermostated saturator with liquid MeOH and N_2 as a carrier gas. The reaction products were analysed with an online Thermo Trace GC equipped with a thermal conductivity detector (TCD) coupled with a PoraPLOT Q pre-column (2 m, 0.32 mm, 20 μm) and Molsieve 5A column (10 m, 0.32 mm) for analysis of permanent gases, a flame ionization detector (FID) equipped with RTX-1 column (2 m, 0.32 mm, 5.00 μm) and Al_2O_3/KCl column (15 m, 0.32 mm, 10 μm) for the analysis of C_1 to C_4 hydrocarbons and the other

FID equipped with RTX-VMS column (30 m, 0.33 mm, 3.00 μm) for C_{5+} hydrocarbons.

Prior to reaction, the catalyst was activated in 50 mL/min air by heating up at 5 °C/min to 550 °C and then cooling down to the reaction temperature 450 °C. The partial pressure of MeOH in the flow was set at 5.2 kPa, corresponding with a weight hourly space velocity (WHSV) of 5.2 $g_{MeOH}·g_{cat}^{-1}$ h^{-1}. The reaction conversion, selectivity and yield were then calculated on a carbon molar basis as follows:

$$X = (\phi_{C,MeOH_{in}} - \phi_{C,MeOH} - 2\phi_{C,DME_{out}})/\phi_{C,MeOH_{in}} \times 100\%$$

$$S_{Cn} = n\phi_{Cn}/(\phi_{C,MeOH_{in}} - \phi_{C,MeOH_{out}} - 2\phi_{C,MeOH_{out}}) \times 100\%$$

$$Y_{Cn} = XS_{Cn}/100$$

where X, ϕ_{Cn}, S_{Cn} and Y_{Cn} represent the carbon-based conversion of MeOH plus dimethyl ether (DME), molar flow rate and carbon selectivity to certain hydrocarbon product in the exhaust with carbon number equal to n and the corresponding carbon yield, respectively. To describe the catalyst deactivation, MeOH conversion capacity [57] was estimated following:

$$R_0 = WHSV_{MeOH} \times t_{0.5}$$

where $WHSV_{MeOH}$ is the weight hourly space velocity of MeOH and $t_{0.5}$ is the catalyst lifetime with MeOH conversion is within 100%–50%.

After catalytic tests, thermogravimetric analysis of the spent catalyst samples was performed on a Mettler Toledo TGA/SDTA 851e TGA analyser. 20 mg spent catalyst was first treated at 200 °C with 20 mL/min air for 1 h to remove water and other volatile species, and then heated in the same air flow up to 800 °C at 5 °C/min while recording the sample mass.

2.6. *Operando UV-vis diffuse reflectance spectroscopy*

Operando UV-vis diffuse reflectance spectra were collected using 60 mg of sieved catalyst (particle size 212–355 μm) in a quartz, rectangular reactor. Details of the set-up can be found elsewhere [58–60]. Prior to reaction and spectra collection, the catalyst was pre-treated at 550 °C in 10 mL/min O_2 for 1 h after which a He flow of 35 mL/min was used to get rid of the O_2. The MTO reaction was carried out at 450 °C by flowing He as a carrier gas (25 mL/min) through a MeOH saturator kept at 21 °C, corresponding with a WHSV of ~5.4 g_{MeOH} g_{cat}^{-1} h^{-1}. During MeOH conversion, *operando* UV-Vis spectra were obtained using an AvaSpec 2048L spectrometer connected to a high-temperature UV-Vis optical fiber probe, which was used to collect spectra in reflection mode. Every minute a spectrum was saved with 100 accumulations of 80 ms exposure time.

3. Results and discussion

3.1. *Physicochemical properties*

Fig. 1 shows the representative XRD patterns for all zeolite materials together with Rietveld refinement and quantitative results in Table S1. XRD patterns of pure MFI samples and MEL-25-S show close agreements with the expected reflections of MFI and MEL phases, respectively [37]. In comparison with MFI samples, the increasing ratio of intensity between the (013) reflection at 23.7° and the (241) reflection at 24.3° in MFI/MEL-25-S and MFI/MEL-50-L confirms the presence of the MEL in the intergrowth samples [39]. The refinement in Table S1 gives the unit cell parameters of all catalysts, which correspond well with the reported values [37]. The XRD data indicate a high crystallinity of all the utilized materials. The crystallinity fraction shows that MFI/MEL-25-S contains 50%/50% of MFI and MEL phase, while MFI/MEL-50-L contains 63%/37% of MFI and MEL phase.

The textural and acidic characteristics of the zeolite catalysts are summarized in Table 1. The chemical compositions give the actual Si to Al ratio in agreement with that as provided. The SEM results (Fig. S1) show that intergrowth MFI/MEL-50-L consists of the largest aggregates with a diameter of 2–5 μm while the other zeolites feature particle sizes below 1 μm. All samples have a similar micropore volume of 0.15–0.16 cm^3/g resulting in similar N_2 adsorption isotherms at $P/P_0 < 0.6$ (Fig. S2). The smallest external surface area (27 m^2/g) is observed for the MFI/MEL-50-L featuring largest crystal size (830 Å, Table 1). The steep uptake of N_2 from $P/P_0 > 0.7$ without an evident hysteresis loop on the samples with the 'S' suffix is in line with the developed external surface area of the smaller-crystallite materials. As a consequence, V_{total}, which is evaluated on the isotherm point at $P/P_0 = 0.95$ shows that samples with the small crystal size exhibit the larger amount of N_2 adsorbed of 0.28–0.31 cm^3 g^{-1} than MFI-25-M (0.22 cm^3/g) and MFI/MEL-50-L (0.19 cm^3 g^{-1}). These results together with the XRD data show that the crystal size varies as follows MFI/MEL-50-L > MFI-25-M > MFI-25-S ≈ MFI-50-S ≈ MEL-25-S ≈ MFI/MEL-25-S.

The acidic properties of the catalysts assessed by FTIR spectroscopy of adsorbed pyridine confirm that the concentrations of BAS in the Si/Al = 25 and 50 samples are consistent with their chemical compositions, while MFI/MEL-25-S contains a higher density of Lewis acid sites (LAS) than the others.

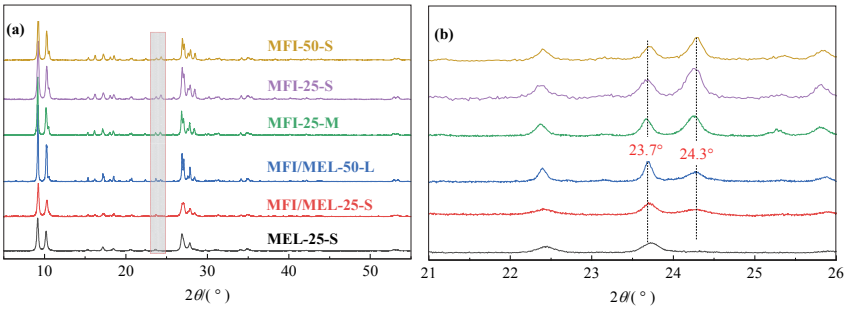

Fig. 1. XRD data comparing patterns for investigated samples (a), and a highlighted 21°–26° range (b).

Table 1
Summarized textural and acidic properties of studied catalysts.

Catalyst	Si/Al [a] (mol mol^{-1})	Size [b] (Å)	V_{total} [c] (cm^3/g)	V_{micro} [c] (cm^3/g)	S_{ext} [c] (m^2/g)	S_{BET} [d] (m^2/g)	BAS [e] (μmol/g)	LAS [e] (μmol/g)
MEL-25-S	27	419	0.31	0.14	85	439	543	90
MFI/MEL-25-S	25	463	0.31	0.15	81	448	556	139
MFI-25-M	26	613	0.22	0.17	56	414	575	94
MFI-25-S	25	428	0.27	0.16	67	453	530	74
MFI/MEL-50-L	48	830	0.19	0.16	27	423	376	72
MFI-50-S	50	428	0.29	0.16	77	471	338	91

[a] Molar ratio determined by ICP-AES. [b] From crystal size analysis on the XRD pattern within 8.4°–9.8° by applying the Scherrer equation. [c] From N_2 adsorption isotherms (Fig. S2) using the t-plot method. [d] From N_2 adsorption isotherms using the BET method. [e] Concentrations of BAS and LAS derived from FT-IR spectroscopy analysis with pyridine as probe (Fig. S3).

The strength of BAS was assessed by FTIR of adsorbed CO. Upon interacting with CO, the downward shift in the OH stretching frequency and the upward shift in the CO vibrations are directly related to the strength of BAS.[61] As shown in Fig. S4, a similar Δν(OH) (310–314 cm^{-1} in Si/Al = 25 and 313–317 cm^{-1} in Si/Al = 50) is observed. Together with the similar C–O stretching shift (35–36 cm^{-1} in Si/Al = 25 and 36–37 cm^{-1} in Si/Al = 50), it indicates an almost identical strength of the BAS for all studied samples [61–64]. BAS with slightly higher strength was characterized for MFI-50-S and MFI/MEL-50-L, which is ascribed to the lower Al concentration in those materials [65,66].

3.2. Catalytic testing

To evaluate the MTO catalytic performance at steady-state conditions, the overall MTO activity and deactivation as defined by cumulative production yields and MeOH conversion capacity [57], for all materials are summarized in Fig. 2. For all catalysts, the main products are categorized into light olefins (ethylene $C_2^=$, propylene $C_3^=$ and butylenes $C_4^=$), C_1–C_4 (methane, ethane, propane and butanes), BTEX (benzene, toluene, ethylbenzene and xylenes), and C_{5+} for undefined hydrocarbons with carbon number higher than 4.

At the initial stage of the reaction full MeOH conversion is achieved. With the increase in cumulative MeOH throughput all catalysts deactivate giving rise to a rapid decrease in conversion due to coke deposition blocking zeolite micropores and the active sites [67]. For all catalysts, except for the shorter lived MFI/MEL-50-L, the propylene selectivity remains constant with TOS till MeOH conversion starts decreasing as shown in Fig. S5. On the other hand, the selectivities to ethylene and BTEX gradually decrease with TOS before MeOH conversion drops. The similar profiles of ethylene and aromatics (BTEX) within the 100% MeOH conversion range further support the mechanistic proposal by Olsbye *et al.* [7] on the role of the aromatics-based cycle for ethylene production.

The MeOH conversion capacity of MFI-50-S is 14.1 $mol_{carbon}/mmol_{BAS}$, which is higher than 7.4 $mol_{carbon}/mmol_{BAS}$ obtained over MFI-25-S, emphasizing the positive impact of the lower Al concentration on the catalyst stability [15]. Regarding the crystallite size, MFI-25-M with relatively larger crystal sizes exhibits a slightly lower conversion capacity (6.6 $mol_{carbon}/mmol_{BAS}$) than its counterpart MFI-25-S (7.4 $mol_{carbon}/mmol_{BAS}$). This is in line with previous observations that mesoporosity development, achieved by either synthesizing nano-sized zeolites or introducing a hierarchical structure, improves the catalyst stability in the MTO process [68–71]. The intergrowth MFI/MEL-25-S and MFI/MEL-50-L catalysts show the lowest MeOH conversion capacity (ca. 5.8 and 6.1 $mol_{carbon}/mmol_{BAS}$, respectively) suggesting the intergrowth of the two zeolite phases increases the catalyst deactivation rate.

The product distributions in the MTO test are evaluated based on the cumulative yields (Fig. 2(b)) and the carbon selectivity at varying MeOH conversion levels (Fig. 3 and Fig. S6).

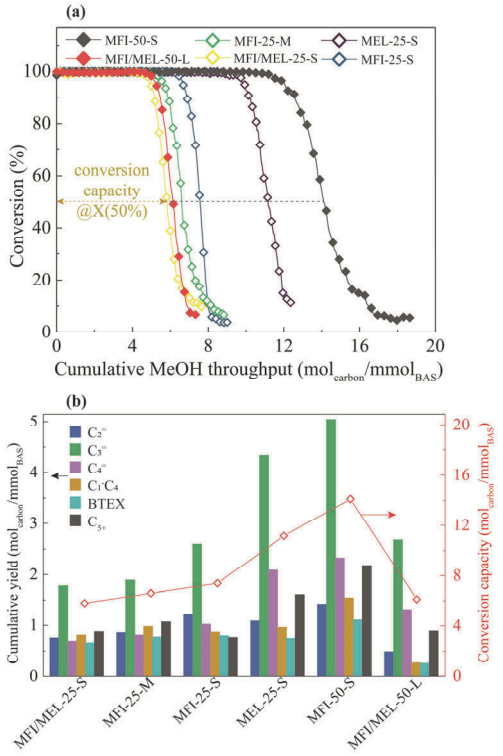

Fig. 2. MeOH conversion as a function of cumulative MeOH throughput (a) and cumulative carbon yields of different hydrocarbons until MeOH conversion is at 50% (color bars) and estimated conversion capacity (symbols to right axis) (b) for all studied catalysts in MTO tests. Reaction conditions: T = 450 °C, m_{cat} = 40 mg (150–212 μm), 1 bar, WHSV = 5.2 g_{MeOH}/g_{cat}/h, carrier gas N_2 = 50 mL/min. The full picture of MeOH conversion and product selectivity curves as a function of TOS are presented in Fig. S5.

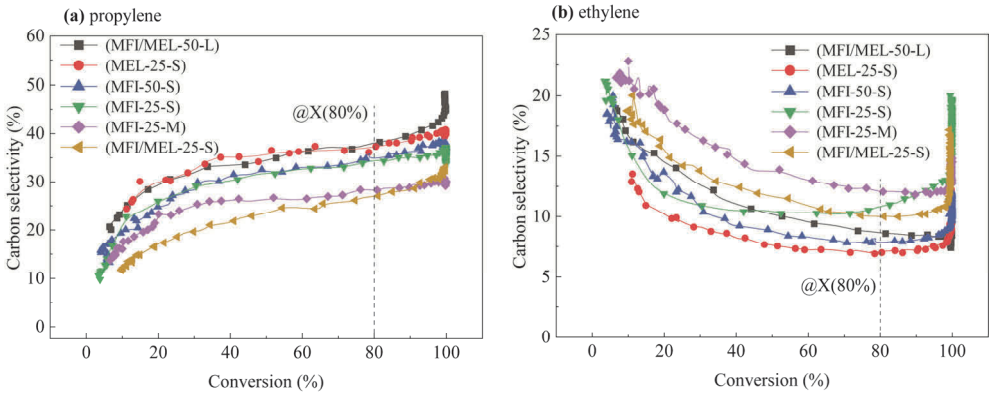

Fig. 3. Carbon selectivity to propylene (a) and ethylene (b) as a function of MeOH conversion over studied materials. Reaction conditions: Reaction conditions: T = 450 °C, m_{cat} = 40 mg (150–212 μm), 1 bar, WHSV = 5.2 g_{MeOH}/g_{cat}/h, carrier gas N_2 = 50 mL/min. Similar graphs of other product groups are presented in Fig. S6.

Previous studies suggest the decrease in conversion in the later stage of the MTO test (gradual deactivation) can be regarded as the change in contact time due to the coke deposition particularly for MFI-type and TON-type zeolites [57,72,73].

For all catalysts, the cumulative yields of propylene and butylenes are higher than other products (Fig. 2(b)), which suggests the olefinic cycle reactions prevail over all materials at studied MTO conditions. Similar to the trend in the MeOH conversion capacity, MEL-25-S has the higher cumulative yield of propylene (4.3 $mol_{carbon}/mmol_{BAS}$) than MFI-25-S, MFI-25-M and MFI/MEL-25-S (2.6, 1.9, and 1.8 $mol_{carbon}/mmol_{BAS}$, respectively) with Si/Al of 25. A similar trend was also observed for samples with Si/Al of 50 emphasizing the impact of catalyst stability on the cumulative yields in the MTO process.

Upon decreasing MeOH conversion, the selectivity to propylene and butylene decreases while that to ethylene gradually increases (Fig. 3 and S6). The latter can be interpreted that more polyaromatic precursors present in the catalyst during the deactivation proceeds the dealkylation to give the ethylene formation. To note, the trends of selectivity towards propylene and ethylene are similar for all catalysts. Only the selectivity to ethylene over MFI-25-S, deviates from this general trend, showing no increase but a more constant level over a MeOH conversion of 80%–20%. This correlates with the decreasing BTEX over that range in contrast to the more constant level for the other samples (Fig. S6). Focusing on the comparison of product distribution over studied materials, the selectivity at MeOH conversion of 80% is chosen as reference in this study.

The selectivity to propylene is 27% and 38% for MFI/MEL-25-S and MFI/MEL-50-L, and 10% and 9% to ethylene, respectively. This is in line with earlier reports showing that a higher lattice Al concentration in MFI enhances the interaction of substituted benzene intermediates with BAS giving rise to the propagation of the aromatics-based cycle and, accordingly, an increased ethylene and BTEX selectivity in the MTO process [25]. In a previous study the total light olefin selectivity in MTO was observed to monotonically increase with the crystal size, attributed to diffusion interference and a higher retention of methylbenzenes [74]. This latter is in line with a higher selectivity to ethylene of MFI-25-M than MFI-25-S in our study. Overall, the observed differences in selectivity levels for the different samples (Fig. 3) point to the importance of other intrinsic catalyst characteristics that define the performance and selectivity of the MTO catalysts.

3.3. *Operando UV-vis spectroscopy*

The active hydrocarbons formed from MeOH and then retained in the zeolite frameworks are defined as the hydrocarbon pool intermediates [75,76]. During the MTO test, *operando* UV-vis spectra of the catalyst were recorded to follow the formation of the retained hydrocarbons. The results are displayed in Fig. 4.

With operando UV-vis spectroscopy, aromatic intermediates in MTO can be determined as well as polyaromatic compounds which act as coke precursors and are thereby deactivating species [12,18,58,59,77]. Only the UV-vis spectra of the first hour of the reaction are represented as after this contributions of broad coke features are increasing in intensity (Fig. S8), which results in a more difficult comparison as the individual absorbance bands are less visible. On all catalysts, three main features including the absorbance bands at ca. 35000, 23000 cm^{-1} and a long tail in the 20000–12000 cm^{-1} are remarkable especially in the first 10 spectra corresponding to TOS up to 10 min. These absorbance bands are assigned, respectively, to neutral methylated benzenes/cyclopentenyl carbocations, methylated benzene/naphthalene carbocations, and (alkylated) polyaromatics. For the MFI-type catalysts, the methylated benzenes with a characteristic absorption band at 35000 cm^{-1} are widely accepted as the active species in the aromatic cycle towards the production of BTEX and ethylene [7,12,77,78], whereas, the polyaromatic species giving rise to the absorbance band in the specified range 20000–12000 cm^{-1} are attributed to coke species [79,80]. The shape of the UV-vis profiles along TOS differs greatly for all studied zeolites, clearly indicating the different features (e.g., density, structure, etc.) of the retained hydrocarbons present in MTO towards the steady-state MTO product distributions. After reacting for 1 h for all zeolites, the bands at 35000 and 23000 cm^{-1} diminished in intensity while the UV-vis absorption in the broad range of 20000–12000 cm^{-1}

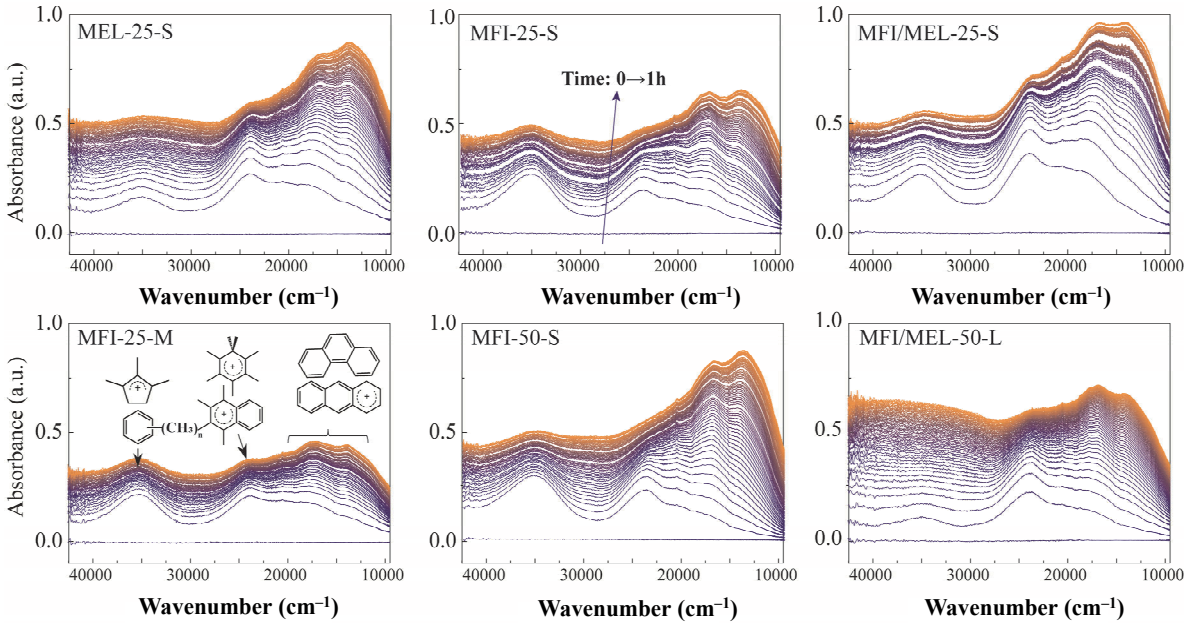

Fig. 4. Time-resolved operando UV-vis spectra during MeOH conversion at 450 °C over studied catalysts. All spectra were collected during TOS within 0–1 h with 1 min interval. Band Assignments in the 40000–12500 cm^{-1} are displayed in UV-vis spectra for MFI-25-M [58,59].

continuously grew, which is related to the accumulation of polyaromatics, probably on the external surface hindering the UV-vis absorption of inner species [77]. Compared with MFI-25-S and MFI/MEL-25-S, the relatively weak UV-vis absorption for methylated benzenes (35000 cm^{-1}) in MEL-25-S is well in line with its high propylene and low ethylene selectivity (Fig. 3), confirming the higher contribution of the olefinic cycle in the dual-cycle mechanism. Additionally, the mediated contribution of methylbenzenes for MFI/MEL-25-S is ascribed to the combination of MFI and MEL structures.

A faster stabilization is observed of the UV-vis absorbance bands for MFI-25-M compared to MFI-25. The relatively higher contribution of polyaromatics (20000–12000 cm^{-1}) for MFI-25-M especially during the first 10 spectra might be related to its faster deactivation than MFI-25-S (Fig. 2), and suggests blocking the access to the larger crystallites of MFI-25-M and hence a lower coke deposition (Fig. S7). When comparing zeolites with the different Si/Al ratios, MFI-50-S shows very similar UV-vis spectra as MFI-25-S, while MFI/MEL-50-L shows a much smaller band at 35000 cm^{-1}, very similar to MEL-25-S in the very early stage of the reaction. A low formation of less methylated benzenes and/or charged monoenyl/cyclopentenyl species (35000 cm^{-1}) compared to the other zeolites, indicates a less pronounced aromatic cycle resulting in a higher propylene selectivity over MFI/MEL-50-L.

3.4. *Effect of external BAS*

The external acid site was characterized by the 1,3,5-TIPB cracking as a probe reaction. The critical diameter of 1,3,5-TIPB (> 8 Å) limits its diffusion into the micropores (< 6 Å) of the zeolites. Thus, the cracking of 1,3,5-TIPB selectively occurs at the external crystal surface. To investigate the effect of external acid sites on MTO stability, the 1,3,5-TIPB cracking results together with MeOH conversion capacity are plotted in Fig. 5.

The 1,3,5-TIPB cracking conversion indicates the different external acid site concentrations for all catalysts. Among the studied catalysts, the negligible cracking activity of MFI/MEL-50-L at 200 °C correlates with its largest crystal size (smallest external surface) and an ultimately low external acid density in comparison with MFI-50-S. The latter is also evidenced by its higher Si/Al at the external surface than MFI-50-S (Table S2). On the contrary, the highest 1,3,5-TIPB conversion of MEL-25-S stands out and suggests the highest concentration of BAS on its external surface. XPS analysis in Fig. S10 and Table S2, however, indicates a lower Al content at the external

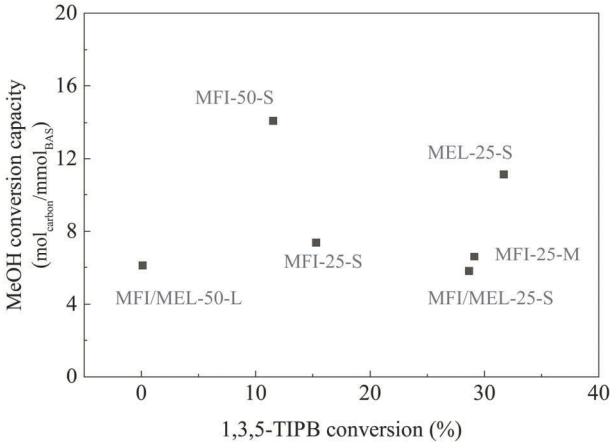

Fig. 5. MeOH conversion capacity as a function of 1,3,5-TIPB conversion over catalysts at 200 °C. Cracking conditions: T = 200 °C, m_{cat} = 20 mg (150–212 μm), 1 bar, $P_{1,3,5\text{-TIPB}}$ = 0.3 kPa, carrier gas N_2 = 50 mL/min. Cracking conversion was averaged within TOS = 0.1–0.3 h. The full picture of 1,3,5-TIPB conversion as a function of TOS were present in Fig. S9.

surface of MEL-25-S than that of MFI-25-M and MFI/MEL-25-S.

Mores *et al.* [81] observed coke deposited on the external BAS in the MTO process blocks the pores for further access to the internal BAS, which causes the catalyst deactivation. However, our results do not present a clear correlation between the concentration of the external BAS and MeOH conversion capacity (Fig. 5). MFI/MEL-50-L showing negligible cracking activity at the outer surface also converts the lowest amount of MeOH before deactivation in the MTO test. Further, the highest MeOH conversion capacity is observed for MEL-25-S, which also shows the highest 1,3,5-TIPB cracking conversion.

3.5. *Effect of aluminium location*

Recent research shows that the isomorphous substitution of T-sites by Al in the zeolite framework is not random [82,83]. Also the BAS facing cavities or channels are associated with different catalytic activities, due to the confinement effects on the intermediates [46,82,84,85]. To probe the Al distribution in the zeolite catalysts and investigate its effect on the MTO performance, three techniques were applied, namely, the UV-vis analysis of Co-ion exchanged catalysts, ^{27}Al MAS NMR, and C6 paraffin (3-MP and *n*-hexane) cracking tests.

3.5.1. *Al pairing*

The Al distribution in the zeolite catalysts was first quantified by combining Co(II) ion exchange and UV-vis spectroscopy analysis. Co(II) exchange allowed quantification of Al pairing and provided an insight into the Al distribution in the framework [49,84]. The comparison of the Al_{pair} fraction and MTO performance (regarding selectivity towards propylene and the MeOH throughput) of all zeolites is presented in Fig. 6.

The results in Fig. 6 and Table S3 point to the very different Al pairing in the studied zeolites. MEL-25-S and intergrowth MFI/MEL-25-S have a large fraction of Al_{pair}, 47% and 46%, respectively. Two MFI-type catalysts, MFI-25-S and MFI-25-M show a similar fraction of Al_{pair}, 29%, and 30%, respectively. MFI-50-S with the lower Al contents has 42% of Al_{pair}, whereas MFI/MEL-50-L has only 13% of framework Al in paired configurations. The location of Al_{pair} sites was further analyzed by deconvoluting the UV-vis spectra of fully dehydrated Co-exchanged samples (Fig. S11) following the procedures reported by Dědeček *et al*. [48, 49] Most of Al_{pair} is located at the intersections, in line with the previous studies. MEL-25-S and intergrowth MFI/MEL-25-S have the higher fraction of Al_{pair} (77%) at the channel intersection sites than 71%–73% for MFI-25-S, MFI-25-M, and MFI-50-S. The MFI/MEL-50-L has 68% Al_{pair} at the channel intersections.

Previous research indicated that Al in pair (able to host the Co^{2+} hexa-aqua-complex during ion exchange) could cooperate during acid-catalyzed reactions such as MTO on BAS [47]. From this perspective, hydrogen transfer and aromatization reactions that require higher activation energy should occur more easily over Al_{pair} leading to more aromatics products and lower selectivity towards propylene. However, such structure-performance correlation is not observed in this study. MEL-25-S containing the highest amount of Al_{pair} (47%) with 77% of them at intersections shows the highest selectivity to propylene, as the typical product from the olefinic cycle in MTO process. Furthermore, results in Fig. 6(b) suggest that the fraction of Al_{pair} also does not correlate with the MeOH conversion capacity. MEL-25-S and MFI/MEL-25-S both contain a relatively high fraction of Al in pair compared to other catalysts. However, MEL-25-S converts the largest amount of MeOH before deactivation, whereas MFI/MEL-25-S converts the smallest amount of MeOH and represents the least stable MTO catalyst in the group of Si/Al = 25 (Fig. 2(a)).

3.5.2. *Al location*

NMR measurements were performed to provide a more general view of Al (no matter pairing or single) at different locations in the framework. Fig. 7 shows two dimensional (2D) ^{27}Al MQ/MAS NMR spectra with corresponding 1D ^{27}Al MAS NMR spectrum on the top in the 65–45 ppm range.

All ^{27}Al MAS NMR spectra contain a broad peak at 65–45 ppm and a low-intensity peak at ~0 ppm, suggesting that most Al atoms are located at tetrahedral sites (T-sites) and few Al atoms at extraframework locations with octahedral coordina-

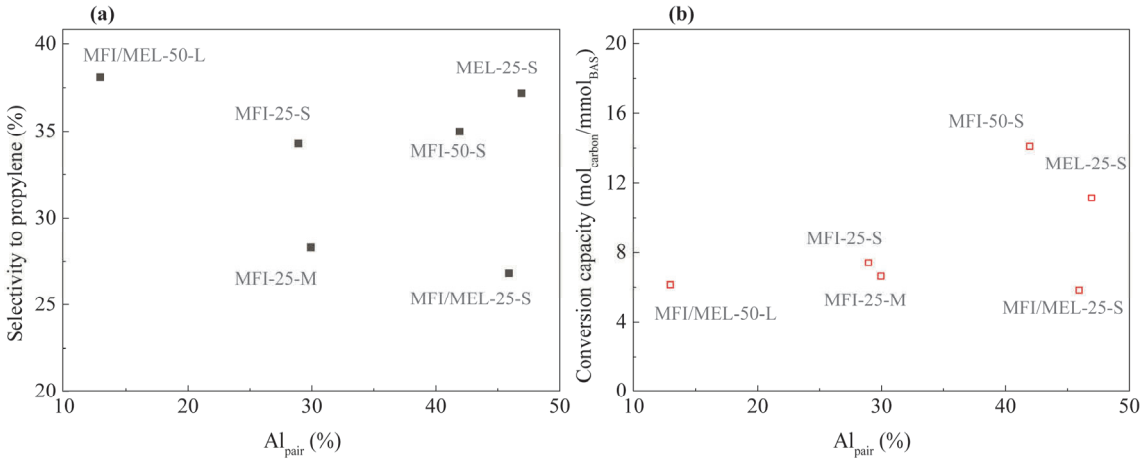

Fig. 6. Selectivity to propylene (a) and MeOH conversion capacity (b) versus the proportion of Al_{pair} of tested samples. Al_{pair} is measured based on Co concentration determined by ICP-AES after Co ion exchange.

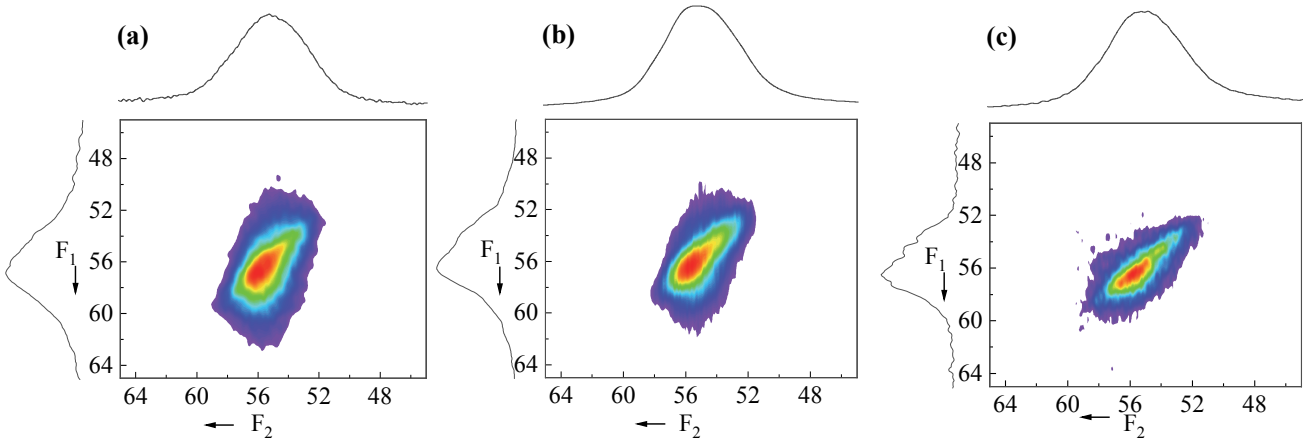

Fig. 7. 2D ^{27}Al MQ MAS NMR spectrum of MEL-25-S (a), MFI-25-M (b), and MFI/MEL-25-S (c) together with the isotopic projection F1 spectrum at the left and the corresponding ^{27}Al MAS NMR spectrum at the top of the 2D contour profile.

tion [64,86]. 2D ^{27}Al MQ MAS NMR spectrum reflects the isotropic chemical shift (δ_{iso}) accompanied by the second-order quadrupolar effect (S_Q) in F1 projection. The ellipsoidal 2D contour and asymmetrical F1 projection clearly show the presence of overlapping signals within 64–45 ppm, which reveals that Al is located at different T-sites in the zeolite unit cell [83]. To distinguish these Al atoms, the broad signal at 65–45 ppm were deconvoluted into five peaks at 58, 56, 55, 54 and 52 ppm. The results are presented in Fig. S12 and the numerical analysis results in Table 2.

Significantly different proportions of the characteristic peaks were obtained for all zeolites (Table 2), which indicate the diverging Al distribution over the different positions in the frameworks.

Based on the combination of the C6 paraffin cracking and ^{27}Al MAS NMR deconvolution results, Yokoi *et al*. [42] attributed the peak at 56 and 53 ppm to the T-sites facing the straight or sinusoidal channels, whereas the signal at 54–55 ppm was assigned to the T-sites of ZSM-5 intersections. A similar assignment for ZSM-11 zeolite was carried on the basis of DFT calculations by Wang *et al*. [33]. Here, the peaks at 56 ppm and 55 ppm were assigned to T-sites facing the straight channels, while the other peaks in the ^{27}Al MAS NMR spectra to the intersection sites of ZSM-11. Following these assignments, our data (Table 2) reveal that in the group with Si/Al 25, MEL-25-S contains the highest fraction of Al in the straight channels. The related MFI-25-S shows a comparable Al distribution with only a slightly higher fraction of Al occupying the intersection sites. The preference for Al sitting at the intersection sites is most pronounced for MFI/MEL-25-S and MFI-25-M samples. At lower Al content, the fraction of Al in the channels slightly increases suggesting a better Al dispersion in the lattice.

The results in Table 2 suggest that the $Al_{channel}$ fraction and selectivity to propylene and butylene (Fig. 3 and S6) correlate well for all studied catalysts. MEL-25-S and MFI/MEL-50-L show the highest selectivities of propylene (35%–36%) and butylenes (16%–18%) in line with their highest fraction of Al in the channels. However, in view of the typical ±5% uncertainty in the deconvolution of ^{27}Al MAS NMR spectra [87], additional characterization of the Al distribution was carried out.

To further distinguish framework Al located in channels or intersections, 3-methylpentane (3-MP) cracking at 400 °C was performed on all catalysts. The location of framework Al was based on the different product selectivity observed, originating from the different transition-state shape selectivity for intersection or channel. Monomolecular 3-MP cracking selectively forms hydrogen, methane, and ethane, whereas the simultaneous bimolecular cracking forms larger carbenium ions and eventually aromatics *via* the classical hydrogen transfer and dehydrogenation reactions and hardly yields products below C3 (Scheme S1). Because bimolecular cracking *via* a bulky transition state is more restricted than monomolecular cracking in the narrow channels of ZSM-5 or ZSM-11, the production level of lower hydrocarbons (methane and ethane) and hydrogen from monomolecular cracking can be used to describe the proportion of Al in the channels [42,88]. 2,4-DMQ was added to avoid unselective cracking at the external crystallite surface.

The shape selectivity of different zeolite topologies for *n*-hexane and 3-MP cracking has also been quantified by the so-called CI presented in Section 2.3 [42,89,90]. In our case, however, the studied materials possess a very similar channel/intersection structure and the sensitivity of this approach becomes less distinctive. Furthermore, the heterogeneous position distribution of lattice Al, shown by ^{27}Al MAS NMR, will affect the cracking mechanism of 3-MP leading to different 3-MP conversions and CI values [42]. As example serves the CI test over MFI-25-S and MEL-25-S here. The *n*-hexane and 3-MP cracking (Fig. S14) over MEL-25-S and MFI-25-S shows that the CI (constraint index) value for MEL-25-S (1.2) is slightly larger than for MFI-25-S (1.0), and would suggest a larger steric hindrance in MEL-25-S than MFI-25-S [42,89,90]. However, this observation is opposite to the fact that the pore size of MEL is slightly larger than MFI. Thus, in this study, CI serves more as a descriptor for a different lattice Al-distribution rather than a steric reactant hindrance of zeolite topology [42].

The overall 3-MP conversion of <5% for all materials is well located in the differential regime, so activity and product selectivity can be directly compared [91]. Accordingly, an excellent correlation between MTO selectivity to propylene and 3-MP cracking selectivity towards hydrogen, methane and ethane is observed for samples with the same Al content (Si/Al = 25 or 50). MEL-25-S shows the highest selectivity towards hydrogen, methane and ethane (55%), whereas MFI-25-M the lowest selectivity (13%). Combined with Table 2, this means that the higher the fraction of Al in channels, the higher the selectivity towards propylene in MTO regardless of the zeolite structure except for MFI/MEL-25-S. Interestingly, an even better correlation between selectivity to propylene and Al fraction at channels is observed when the selectivity at steady-state conditions (MeOH conversion of 100% at TOS of 1 h in Fig. S5) is chosen for all catalysts, in which MFI/MEL-25-S exhibits a higher selectivity to propylene than MFI-25-M.

These results correlate well with the deconvolution results from ^{27}Al MAS NMR, which also indicates a higher fraction of Al in the channels on MEL-25-S than on MFI-25-M. An indicative trend between MTO propylene selectivity (activity of olefinic cycle) and Al location in the channel from NMR and from 3-MP cracking is also found for the samples with Si/Al of 50. With the lower Al content of MFI-50-S and MFI/MEL-50-L, the bimolecular cracking of 3-MP is a more dominant pathway because of the much lower activation energy [54], resulting in selectivity towards methane, ethane and hydrogen below 17%. This also accounts for the higher total 3-MP conversion data (Table S4) for the samples (Si/Al = 25) with a higher Al fraction in the intersections (Table 2). The exceptional case is MFI-50-S. It exhibits the second highest 3-MP conversion of 3.3% among all studied materials, which might indicate the extraordinarily high proportion of Al located at the intersection and the lower selectivity to propylene than MFI/MEL-50-L.

3.6. Discussion

The objective of this study was to reveal key performance parameters of three 10-MR zeolite catalysts, *viz.* MFI, MEL, and a mixed MFI/MEL structure, in the MTO reaction, with the focus on MTO activity, product selectivity (propylene) and stability for two Si/Al ratios. MEL has a similar channel/intersection system as MFI with similar (slightly larger) nano-scale dimensions, but with only straight channels, while MFI/MEL samples contain an MFI and MEL intergrowth structure, which is more than simply a physical mixture.

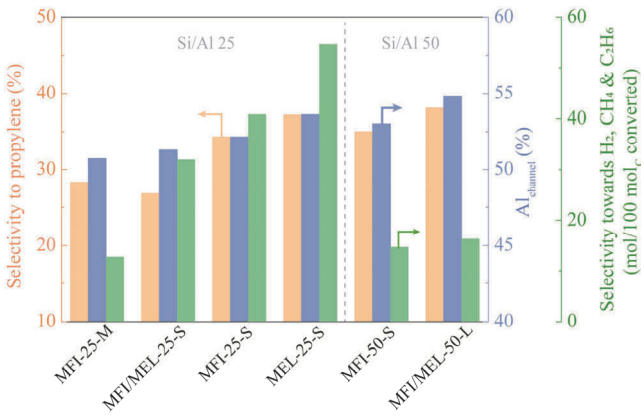

Fig. 8. Carbon selectivity to propylene versus selectivity towards hydrogen, methane and ethane of 3-MP monomolecular cracking over samples with Si/Al of 25 (a) and Si/Al of 50 (b). 3-MP cracking conditions: T = 400 °C, m_{cat} = 20 mg (150–212 μm), 1 bar, carrier gas N_2 = 50 mL/min, 3-MP partial pressure = 3.8 kPa in the presence of 2,4-DMQ (<0.1 kPa). The product selectivity is averaged values within TOS = 0.1–0.4 h. The full-scale picture along TOS is given in Fig. S13.

MTO tests and *operando* UV-vis spectroscopy measurements reveal completely different product distributions and MTO lifetimes coupled with the different features of retained hydrocarbons in all three zeolite structures. With the same Al content (origin of the BAS) and BAS strength, the MEL-type zeolite is shown as the most propylene-selective catalyst in the MTO test, which is in line with reported observations [33,92]. Unlike the shorter MTO lifetime of MEL-type zeolites than of MFI-type zeolites in [33], in our study MEL-25-S exhibits the highest MeOH conversion capacity, more than 50% higher than MFI-25-S and MFI/MEL-25-S. On the other hand, MFI/MEL-50-L shows the higher selectivity to propylene than MFI-50-S. Even two MFI-type samples with Si/Al of 25 exhibit different MTO performance regarding conversion capacity and product selectivity. All these observations indicate that besides the zeolite topology and Al content (BAS density) other parameters are involved in controlling their catalytic performance.

Of the various techniques applied only the 3-MP cracking, and the ^{27}Al MAS NMR spectra analysis revealed a clear correlation between the propylene selectivity in MTO with the Al located in the channels of the zeolites, regardless of zeolite framework and crystal size (Fig. 8): the more Al located in the channels, the higher the selectivity to propylene and butylenes is observed. This seems the primary key performance parameter in this reaction. This suggests that 1D 10-MR zeolites, con-

Table 2
The fraction of various peaks obtained from the ^{27}Al MAS NMR spectrum.

Catalyst	$Al_{intersection}$/%	$Al_{channel}$/%	Characteristic peaks proportion/%				
			58±0.3 ppm	56±0.2 ppm	55±0.5 ppm	53±0.4 ppm	52±0.3 ppm
MEL-25-S	46.4	53.6	11.1	24.0	29.6	24.1	11.2
MFI-25-S	47.9	52.1	9.0	28.6	24.2	23.6	14.7
MFI/MEL-25-S	48.7*	51.3*	14.2	25.0	28.6	24.1	8.2
MFI-25-M	49.3	50.7	11.7	25.5	24.8	25.3	12.7
MFI-50-S	47.0	53.0	8.0	26.9	25.5	26.1	13.5
MFI/MEL-50-L	45.2*	54.8*	15.3	32.1	31.8	18.3	2.5

* Al proportions for intergrowth samples were calculated based on the fraction of MFI and MEL phase in Table S1.

taining only channels would be the preferred catalysts, completely suppressing the aromatics-based cycle. Indeed, no aromatic products were observed for ZSM-22 and ZSM-23 catalysts, although ZSM-48 with slightly wider channels did [73,93]. Aromatics were formed in all catalysts, but were trapped in the former systems and only could diffuse out of the latter, similarly as for 1D 12-MR ZSM-12 [94]. Comparing ZSM-22 with ZSM-5 and ZSM-11 revealed, however, a lower propylene selectivity, ~38% versus ~50%, and a much shorter lifetime [26]. Introduction of mesoporosity by desilication and acid treatment doubled the ZSM-22 lifetime with retained shape selectivity [33], suggesting an easier escape of coke precursors like in the case of ZSM-48 [73]. So, the high propylene and butylene selectivity of the 10-MR MEL-25-S is attributed to its high fraction of Al located in the channels, similar as for the mixed phase MFI/MEL-50-L. The latter has the highest light olefin selectivity, indicating that an optimal BAS concentration exists for an optimal performance [31]. Our results confirm the results of Wang *et al*. [33] observing and Al enrichment in the intersections of ZSM-5 and in the channels of ZSM-11. We further extend this rule to the intergrowth MFI/MEL samples. These findings provide a rational basis for the targeted synthesis of 3D 10-MR zeolites with only Al located in the channels for improved olefin production. An enrichment of Al in the channels was indeed obtained by Li *et al*. [82] by preparation of B-Al-ZSM-5 and removal of B that preferentially resided in the intersections. This indeed improved the propylene and butylene selectivity in MTO. These post-synthesis approaches confirm the attempts to concentrate Al in the channels of ZSM-5 (or remove it from the intersections) to improve the MeOH selectivity towards the lower olefins, in agreement with the results for theta-1 (TON-type, 1D zeolite) [34,95].

The correlation between Al located in the channels and MeOH selectivity towards propylene (or light olefins) holds for all three zeolite structures, which further suggests the Al location is a more significant factor than zeolite structure, at least among MFI, MEL, and MFI/MEL in MTO, while other properties (crystal size, Al-content and external BAS) are of secondary influence (less pronounced), affecting selectivity, coke deposition, and time-on-stream MTO activity.

It is rather difficult to determine a single key parameter controlling the MTO deactivation in this study. Smaller crystals provide shorter diffusion distances for (poly)aromatics to escape and a larger external area (capacity) for coke deposition. In larger crystals, the lower coke deposition in the outer crystal regions can limit accessibility to the BAS resulting in a faster deactivation and less coke. This might also explain the fast deactivation for MFI-25-M in comparison with other catalysts with the smaller crystal size.

Co(II) ion-exchange coupled with *ex-situ* UV-vis analysis reveals that a large fraction of Al_{pair} is located in the intersection regardless of Si/Al and zeolite structure. But there is no clear correlation between Al_{pair} information (fraction or location) with the MTO deactivation. Both MEL and MFI/MEL catalysts with the same Al content contain ca. 46% Al_{pair} with more than 70% of them in the intersection, but the MEL-type zeolite is shown as the most stable, while MFI/MEL-25-S the least stable catalyst in the MTO test (Fig. 2). Another notorious example is MFI/MEL-50-L, which contains the smallest fraction of Al_{pair} but deactivates quickly in MTO. By applying 1,3,5-TIPB cracking, probing the acidity on the external surface of the samples, combined with XPS analysis (Table S2), a heterogeneous distribution of Al within the zeolite particle is observed. As the uncontrolled alkylation of hydrocarbons leading to coke deposition on the external BAS in MTO could block the pores for further access to the internal active sites [81], a less acidic outer surface expectedly correlates with the longer MTO lifetime and vice-versa. It explains the exceptionally high level of external BAS coupled with the low MeOH conversion capacity on MFI-25-M (Fig. 5). The intergrowth sample with Si/Al of 25 shows the highest level of external BAS, corresponding with the lowest MeOH conversion capacity (Fig. 5) in comparison with the MFI-type and MEL-type samples with the same Al content and crystal size. However, MEL-25-S exceptionally contains a higher fraction of external BAS but shows a higher MeOH conversion capacity than MFI-25-S, while MFI/MEL-50-L shows negligible external BAS coupled with a much lower MeOH conversion capacity than MFI-50-S. Clearly, the impact of Al distribution in the framework cannot be ignored. The MTO deactivation is closely related to the activity of the aromatic-based cycle, as polyaromatics are commonly described as the coke species. The higher level of Al located in the channels not only directs the MeOH selectivity towards light olefins, but also reduces the contribution of the competing aromatic-based cycle eventually leading to polyaromatics deposition. This might explain the high production of light olefins coupled with the largest MeOH conversion capacity for the MEL-type catalyst.

4. Conclusions

The property-performance relationship in the MTO process for three zeolite structures of MFI, MEL, and intergrowth MFI/MEL were evaluated *via* a series of characterization techniques and probe reactions. The MTO test combined with *operando* UV–vis spectroscopy shows that product selectivity, MeOH conversion capacity, and retained hydrocarbons before deactivation are significantly different for the studied zeolites. Besides the morphology and Al content, more intrinsic aspects concerning Al distribution were revealed and their correlations with the catalytic performance were discussed. Through ^{27}Al MAS NMR analysis and 3-MP cracking, an excellent correlation between Al location and MeOH selectivity towards propylene and butylenes is observed regardless of the different zeolite frameworks. The higher level of Al located in the channels (straight or sinusoidal) suppresses the propagation of the aromatic cycle, which requires spacious space like intersections, and favours the olefinic cycle. Therefore, the MeOH selectivity towards C_3–C_4 light olefins is considerably improved for MEL-type and one MFI/MEL intergrowth zeolite containing the highest fraction of Al in the channels. The intergrowth of MFI and MEL phases accelerates the catalyst deactivation rate evidenced by the lowest MeOH conversion capacities in the MTO process.

Other zeolite parameters as Al_{pair} and external BAS concen-

tration, evaluated *via* Co ion-exchange technique and 1,3,5-TIPB cracking, showed lack of a clear correlation with MeOH selectivity and suggests these parameters are of less pronounced influence on product distribution, specifically the production of propylene. No correlation between these parameters and MeOH conversion capacity was obtained, revealing MTO deactivation is a rather complex process, which cannot be captured by a single parameter. Crystal size, Al-content, external BAS and Al-distribution in the framework all affect the deactivation. All these characterizations and probe reactions still comprise part of catalyst properties that potentially affect the catalytic performance. More key parameters, such as diffusivity within the zeolite micropore [96] are not analysed quantitatively in this study, but their impact on the MTO mechanism especially for the intergrowth MFI/MEL samples cannot be ignored.

This work not only provides the direct relationship between zeolite acidic properties and their catalytic influence in the MTO process benefiting the rational catalyst design for the MTO process but also reveals that methanol transformation in the zeolite is an extremely complex process, which is affected by multiple parameters to a different level. Our study also highlights the importance of an integrated approach to characterize and analyse all intrinsic properties of zeolite catalysts in the MTO process.

Acknowledgment

We acknowledge BASF and the Advanced Research Center Chemical Building Blocks Consortium (ARC CBBC) for funding under project number 2016.007.TUD.

Electronic supporting information

Supporting information is available in the online version of this article.

References

[1] G. A. Olah, *Angew. Chem. Int. Ed.*, **2005**, 44, 2636–2639.
[2] G. A. Olah, A. Goeppert, G. S. Prakash, *J. Org. Chem.*, **2008**, 74, 487–498.
[3] F. M. Mota, D. H. Kim, *Chem. Soc. Rev.*, **2019**, 48, 205–259.
[4] F. J. Keil, *Microporous Mesoporous Mater.*, **1999**, 29, 49–66.
[5] P. Tian, Y. Wei, M. Ye, Z. Liu, *ACS Catal.*, **2015**, 5, 1922–1938.
[6] Z. Xie, J. Liu, S. Zhong, H. Zhang, *Process for producing light olefins from methanol or dimethyl ether*, U.S.P.a.T. Office, Editor. **2014**, China Petroleum and Chemical Corp Sinopec Shanghai Research Institute of Petrochemical Technology.
[7] S. Svelle, F. Joensen, J. Nerlov, U. Olsbye, K.-P. Lillerud, S. Kolboe, M. Bjørgen, *J. Am. Chem. Soc.*, **2006**, 128, 14770–14771.
[8] S. Xu, A. Zheng, Y. Wei, J. Chen, J. Li, Y. Chu, M. Zhang, Q. Wang, Y.

Graphical Abstract

Chin. J. Catal., 2022, 43: 1879–1893 doi: 10.1016/S1872-2067(21)63990-6

An integrated approach to the key parameters in methanol-to-olefins reaction catalyzed by MFI/MEL zeolite materials

Chuncheng Liu, Evgeny A. Uslamin, Sophie H. van Vreeswijk, Irina Yarulina, Swapna Ganapathy, Bert M. Weckhuysen, Freek Kapteijn *, Evgeny A. Pidko *
Delft University of Technology, the Netherlands; Process Research and Chemical Engineering, Germany; Utrecht University, the Netherlands

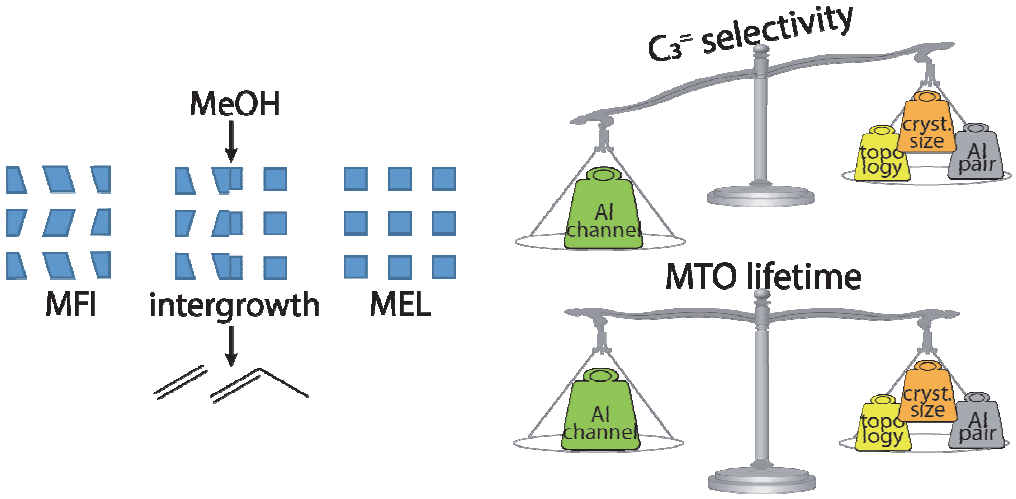

Al enrichment in the channels is of primary importance to determine propylene production in MTO. Catalyst deactivation is rather complex, which is controlled by Al distribution, crystal size, topology and Al_{pair}.

Zhou, J. Wang, F. Deng, Z. Liu, *Angew. Chem. Int. Ed.*, **2013**, 52, 11564–11568.
[9] U. Olsbye, S. Svelle, K. Lillerud, Z. Wei, Y. Chen, J. Li, J. Wang, W. Fan, *Chem. Soc. Rev.*, **2015**, 44, 7155–7176.
[10] X. Wu, S. Xu, W. Zhang, J. Huang, J. Li, B. Yu, Y. Wei, Z. Liu, *Angew. Chem. Int. Ed.*, **2017**, 56, 9039–9043.
[11] C. Li, C. Paris, J. Martinez-Triguero, M. Boronat, M. Moliner, A. Corma, *Nat. Catal.*, **2018**, 1, 547–554.
[12] I. Yarulina, K. De Wispelaere, S. Bailleul, J. Goetze, M. Radersma, E. Abou-Hamad, I. Vollmer, M. Goesten, B. Mezari, E. J. M. Hensen, J. S. Martínez-Espín, M. Morten, S. Mitchell, J. Perez-Ramirez, U. Olsbye, B. M. Weckhuysen, V. Van Speybroeck, F. Kapteijn, J. Gascon, *Nat. Chem.*, **2018**, 10, 804–812.
[13] D. M. McCann, D. Lesthaeghe, P. W. Kletnieks, D. R. Guenther, M. J. Hayman, V. Van Speybroeck, M. Waroquier, J. F. Haw, *Angew. Chem. Int. Ed.*, **2008**, 47, 5179–5182.
[14] S. Ilias, A. Bhan, *J. Catal.*, **2012**, 290, 186–192.
[15] A. Hwang, A. Bhan, *Acc. Chem. Res.*, **2019**, 52, 2647–2656.
[16] I. Yarulina, A. D. Chowdhury, F. Meirer, B. M. Weckhuysen, J. Gascon, *Nat. Catal.*, **2018**, 1, 398–411.
[17] M. Stöcker, *Microporous Mesoporous Mater.*, **1999**, 29, 3–48.
[18] U. Olsbye, S. Svelle, M. Bjørgen, P. Beato, T. V. W. Janssens, F. Joensen, S. Bordiga, K. P. Lillerud, *Angew. Chem. Int. Ed.*, **2012**, 51, 5810–5831.
[19] S. Ilias, A. Bhan, *ACS Catal.*, **2013**, 3, 18–31.
[20] M. Bjørgen, U. Olsbye, D. Petersen, S. Kolboe, *J. Catal.*, **2004**, 221, 1–10.
[21] W. Song, H. Fu, J. F. Haw, *J. Am. Chem. Soc.*, **2001**, 123, 4749–4754.
[22] U. Olsbye, S. Svelle, M. Bjørgen, P. Beato, T. V. Janssens, F. Joensen, S. Bordiga, K. P. Lillerud, *Angew. Chem. Int. Ed.*, **2012**, 51, 5810–5831.
[23] S. Svelle, F. Joensen, J. Nerlov, U. Olsbye, K.-P. Lillerud, S. Kolboe, M. Bjørgen, *J. Am. Chem. Soc.*, **2006**, 128, 14770–14771.
[24] S. Ilias, R. Khare, A. Malek, A. Bhan, *J. Catal.*, **2013**, 303, 135–140.
[25] R. Khare, Z. Liu, Y. Han, A. Bhan, *J. Catal.*, **2017**, 348, 300–305.
[26] R. Wei, C. Li, C. Yang, H. Shan, *J. Nat. Gas Chem.*, **2011**, 20, 261–265.
[27] N. Danilina, F. Krumeich, S. A. Castelanelli, J. A. van Bokhoven, *J. Phys. Chem. C*, **2010**, 114, 6640–6645.
[28] V. Pashkova, S. Sklenak, P. Klein, M. Urbanova, J. Dedecek, *Chem. Eur. J.*, **2016**, 22, 3937–3941.
[29] B. Smit, T. L. Maesen, *Nature*, **2008**, 451, 671–678.
[30] B. P. Hereijgers, F. Bleken, M. H. Nilsen, S. Svelle, K.-P. Lillerud, M. Bjørgen, B. M. Weckhuysen, U. Olsbye, *J. Catal.*, **2009**, 264, 77–87.
[31] M. Dyballa, P. Becker, D. Trefz, E. Klemm, A. Fischer, H. Jakob, M. Hunger, *Appl. Catal. A*, **2016**, 510, 233–243.
[32] Q. Yu, C. Cui, Q. Zhang, J. Chen, Y. Li, J. Sun, C. Li, Q. Cui, C. Yang, H. Shan, *J. Energy Chem.*, **2013**, 22, 761–768.
[33] S. Wang, P. Wang, Z. Qin, Y. Chen, M. Dong, J. Li, K. Zhang, P. Liu, J. Wang, W. Fan, *ACS Catal.*, **2018**, 8, 5485–5505.
[34] M. Dyballa, U. Obenaus, M. Rosenberger, A. Fischer, H. Jakob, E. Klemm, M. Hunger, *Microporous Mesoporous Mater.*, **2016**, 233, 26–30.
[35] S. Teketel, U. Olsbye, K. P. Lillerud, P. Beato, S. Svelle, *Appl. Catal. A*, **2015**, 494, 68–76.
[36] J. Wang, Y. Wei, J. Li, S. Xu, W. Zhang, Y. He, J. Chen, M. Zhang, A. Zheng, F. Deng, *Catal. Sci. Technol.*, **2016**, 6, 89–97.
[37] C. Baerlocher, L. B. McCusker, Database of Zeolite Structures: http://www.iza-structure.org/databases, **2019**.
[38] G. R. Millward, S. Ramdas, J. M. Thomas, M. T. Barlow, *J. Chem. Soc., Faraday Trans. 2*, **1983**, 79, 1075–1082.
[39] M. Conte, B. Xu, T. E. Davies, J. K. Bartley, A. F. Carley, S. H. Taylor, K. Khalid, G. J. Hutchings, *Microporous Mesoporous Mater.*, **2012**, 164, 207–213.
[40] J. Zhong, J. Han, Y. Wei, Z. Liu, *J. Catal.*, **2021**, 396, 23–31.
[41] C. Emeis, *J. Catal.*, **1993**, 141, 347–354.
[42] T. Yokoi, H. Mochizuki, S. Namba, J. N. Kondo, T. Tatsumi, *J. Phys. Chem. C*, **2015**, 119, 15303–15315.
[43] L. Petrakis, *J. Chem. Edu.*, **1967**, 44, 432–436.
[44] K. Chen, *Int. J. Mol. Sci.*, **2020**, 21, 5666.
[45] J. Holzinger, P. Beato, L. F. Lundegaard, J. Skibsted, *J. Phys. Chem. C*, **2018**, 122, 15595–15613.
[46] T. Liang, J. Chen, Z. Qin, J. Li, P. Wang, S. Wang, G. Wang, M. Dong, W. Fan, J. Wang, *ACS Catal.*, **2016**, 6, 7311–7325.
[47] J. Dedecek, E. Tabor, S. Sklenak, *ChemSusChem*, **2019**, 12, 556–576.
[48] J. Dedecek, D. Kaucky, B. Wichterlova, *Microporous Mesoporous Mater.*, **2000**, 35–36, 483–494.
[49] J. Dedecek, D. Kaucky, B. Wichterlova, O. Gonsiorova, *Phys. Chem. Chem. Phys.*, **2002**, 4, 5406–5413.
[50] A. A. Verberckmoes, B. M. Weckhuysen, R. A. Schoonheydt, *Microporous Mesoporous Mater.*, **1998**, 22, 165–178.
[51] E. Tabor, M. Bernauer, B. Wichterlova, J. Dedecek, *Catal. Sci. Technol.*, **2019**, 9, 4262–4275.
[52] S. Namba, S. Nakanishi, T. Yashima, *J. Catal.*, **1984**, 88, 505–508.
[53] S. Namba, A. Inaka, T. Yashima, *Zeolites*, **1986**, 6, 107–110.
[54] H. Krannila, W. O. Haag, B. C. Gates, *J. Catal.*, **1992**, 135, 115–124.
[55] W. O. Haag, R. M. Lago, P. B. Weisz, *Faraday Discus. Chem. Soc.*, **1981**, 72, 317–330.
[56] V. J. Frillette, W. O. Haag, R. M. Lago, *J. Catal.*, **1981**, 67, 218–222.
[57] T. V. W. Janssens, *J. Catal.*, **2009**, 264, 130–137.
[58] J. Goetze, F. Meirer, I. Yarulina, J. Gascon, F. Kapteijn, J. Ruiz-Martínez, B. M. Weckhuysen, *ACS Catal.*, **2017**, 7, 4033–4046.
[59] E. Borodina, H. Sharbini Harun Kamaluddin, F. Meirer, M. Mokhtar, A. M. Asiri, S. Al-Thabaiti, S. N. Basahel, J. Ruiz-Martinez, B. Weckhuysen, *ACS Catal.*, **2017**, 7, 5268–5281.
[60] T. X. Nijhuis, S. J. Tinnemans, T. Visser, B. M. Weckhuysen, *Phys. Chem. Chem. Phys.*, **2003**, 5, 4361–4365.
[61] S. Bordiga, C. Lamberti, F. Bonino, A. Travert, F. Thibault-Starzyk, *Chem. Soc. Rev.*, **2015**, 44, 7262–7341.
[62] P. Nachtigall, M. R. Delgado, D. Nachtigallova, C. O. Areán, *Phys. Chem. Chem. Phys.*, **2012**, 14, 1552–1569.
[63] S. M. T. Almutairi, B. Mezari, E. A. Pidko, P. C. M. M. Magusin, E. J. M. Hensen, *J. Catal.*, **2013**, 307, 194–203.
[64] A. A. Gabrienko, I. G. Danilova, S. S. Arzumanov, L. V. Pirutko, D. Freude, A. G. Stepanov, *J. Phys. Chem. C*, **2018**, 122, 25386–25395.
[65] J. Dwyer, F. Fitch, E. Nkang, *J. Phys. Chem.*, **1983**, 87, 5402–5404.
[66] C. Liu, G. Li, E. J. Hensen, E. A. Pidko, *J. Catal.*, **2016**, 344, 570–577.
[67] N. Wang, Y. Zhi, Y. Wei, W. Zhang, Z. Liu, J. Huang, T. Sun, S. Xu, S. Lin, Y. He, *Nat. Commun.*, **2020**, 11, 1079.
[68] S. Hu, J. Shan, Q. Zhang, Y. Wang, Y. Liu, Y. Gong, Z. Wu, T. Dou, *Appl. Catal. A*, **2012**, 445–446, 215–220.
[69] M. Y. Jeon, D. Kim, P. Kumar, P. S. Lee, N. Rangnekar, P. Bai, M. Shete, B. Elyassi, H. S. Lee, K. Narasimharao, *Nature*, **2017**, 543, 690–694.
[70] C. Mei, P. Wen, Z. Liu, H. Liu, Y. Wang, W. Yang, Z. Xie, W. Hua, Z. Gao, *J. Catal.*, **2008**, 258, 243–249.
[71] L. Wu, V. Degirmenci, P. C. M. M. Magusin, N. J. H. G. M. Lousberg, E. J. M. Hensen, *J. Catal.*, **2013**, 298, 27–40.
[72] F. L. Bleken, S. Chavan, U. Olsbye, M. Boltz, F. Ocampo, B. Louis, *Appl. Catal. A*, **2012**, 447–448, 178–185.
[73] S. Teketel, W. Skistad, S. Benard, U. Olsbye, K. P. Lillerud, P. Beato, S. Svelle, *ACS Catal.*, **2012**, 2, 26–37.
[74] R. Khare, D. Millar, A. Bhan, *J. Catal.*, **2015**, 321, 23–31.
[75] B. Arstad, S. Kolboe, *J. Am. Chem. Soc.*, **2001**, 123, 8137–8138.

[76] M. Bjørgen, F. Bonino, B. Arstad, S. Kolboe, K. P. Lillerud, A. Zecchina, S. Bordiga, *ChemPhysChem*, **2005**, 6, 232–235.
[77] J. Goetze, B. M. Weckhuysen, *Catal. Sci. Technol.*, **2018**, 8, 1632–1644.
[78] C. Wang, J. Xu, G. Qi, Y. Gong, W. Wang, P. Gao, Q. Wang, N. Feng, X. Liu, F. Deng, *J. Catal.*, **2015**, 332, 127–137.
[79] L. Palumbo, F. Bonino, P. Beato, M. Bjørgen, A. Zecchina, S. Bordiga, *J. Phys. Chem. C*, **2008**, 112, 9710–9716.
[80] M. Bjørgen, S. Svelle, F. Joensen, J. Nerlov, S. Kolboe, F. Bonino, L. Palumbo, S. Bordiga, U. Olsbye, *J. Catal.*, **2007**, 249, 195–207.
[81] D. Mores, E. Stavitski, M. H. F. Kox, J. Kornatowski, U. Olsbye, B. M. Weckhuysen, *Chem. Eur. J.*, **2008**, 14, 11320–11327.
[82] C. Li, A. Vidal-Moya, P. J. Miguel, J. Dedecek, M. Boronat, A. Corma, *ACS Catal.*, **2018**, 8, 7688–7697.
[83] O. H. Han, C.-S. Kim, S. B. Hong, *Angew. Chem. Int. Ed.*, **2002**, 41, 469–472.
[84] J. Dedecek, Z. Sobalík, B. Wichterlová, *Catal. Rev. Sci. Eng.*, **2012**, 54, 135–223.
[85] S. Wang, Y. Chen, Z. Wei, Z. Qin, H. Ma, M. Dong, J. Li, W. Fan, J. Wang, *J. Phys. Chem. C*, **2015**, 119, 28482–28498.
[86] P. Sarv, C. Fernandez, J.-P. Amoureux, K. Keskinen, *J. Phys. Chem.*, **1996**, 100, 19223–19226.
[87] J. Dedecek, M. J. Lucero, C. Li, F. Gao, P. Klein, M. Urbanova, Z. Tvaruzkova, P. Sazama, S. Sklenak, *J. Phys. Chem. C*, **2011**, 115, 11056–11064.
[88] K. Kubo, H. Iida, S. Namba, A. Igarashi, *J. Japan Petroleum Institute*, **2018**, 61, 10–19.
[89] T. Imyen, W. Wannapakdee, J. Limtrakul, C. Wattanakit, *Fuel*, **2019**, 254, 115593.
[90] P. Voogd, H. Van Bekkum, *Appl. Catal.*, **1990**, 59, 311–331.
[91] M. Zhang, M. Wang, B. Xu, D. Ma, *Joule*, **2019**, 3, 2876–2883.
[92] F. Bleken, W. Skistad, K. Barbera, M. Kustova, S. Bordiga, P. Beato, K. P. Lillerud, S. Svelle, U. Olsbye, *Phys. Chem. Chem. Phys.*, **2011**, 13, 2539–2549.
[93] S. Teketel, U. Olsbye, K.-P. Lillerud, P. Beato, S. Svelle, *Microporous Mesoporous Mater.*, **2010**, 136, 33–41.
[94] Z. Liu, Y. Chu, X. Tang, L. Huang, G. Li, X. Yi, A. Zheng, *J. Phys. Chem. C*, **2017**, 121, 22872–22882.
[95] A. K. Jamil, O. Muraza, M. Yoshioka, A. M. Al-Amer, Z. H. Yamani, T. Yokoi, *Ind. Eng. Chem. Res.*, **2014**, 53, 19498–19505.
[96] P. Cnudde, R. Demuynck, S. Vandenbrande, M. Waroquier, G. Sastre, V. V. Speybroeck, *J. Am. Chem. Soc.*, **2020**, 142, 6007–6017.

MFI/MEL分子筛催化甲醇制烯烃反应关键参数的集成方法

Chuncheng Liu [a,d], Evgeny A. Uslamin [a], Sophie H. van Vreeswijk [c], Irina Yarulina [b], Swapna Ganapathy [c], Bert M. Weckhuysen [c], Freek Kapteijn [d,*], Evgeny A. Pidko [a,#]

[a]代尔夫特理工大学化学工程系, 无机系统工程, 代尔夫特, 荷兰
[b]巴斯夫股份公司, 工艺研究和化学工程, 路德维希港, 德国
[c]乌特勒克大学德拜纳米材料科学研究所, 无机化学与催化, 乌特勒克, 荷兰
[d]代尔夫特理工大学化工系, 催化工程系, 代尔夫特, 荷兰

摘要: 了解与关键催化性能参数(如选择性和稳定性)相关的催化剂特性对于合理设计催化剂是非常重要的. 本文重点考察了甲醇制烯烃(MTO)过程中MFI、MEL及其共生沸石分子筛的催化行为和构效关系. 表征结果表明, 丙烯和丁烯的高产率和MeOH的高转化率均与Pentasil分子筛结构中晶格Al位的富集相关, 这也被27Al MAS NMR结果和3-甲基戊烷裂解结果证实. 催化剂对MTO反应的催化性能与其晶体尺寸、外部B酸中心和铝配对等性质之间缺乏相关性, 表明它们对提高丙烯选择性的作用不大. 本文分析表明, 催化剂失活非常复杂, 受交叉点处晶格铝富集、总铝含量和晶体尺寸影响较大, 且MFI和MEL相共生加速了催化剂失活.

关键词: 构效关系; 分子筛催化; 甲醇制烯烃; 铝分布; 酸性; 共生MFI/MEL; Pentasil分子筛

收稿日期: 2021-11-08. 接受日期: 2021-12-04. 上网时间: 2022-05-20.
*通讯联系人. 电子信箱: F.Kapteijn@tudelft.nl
#通讯联系人. 电子信箱: e.a.pidko@tudelft.nl
本文的电子版全文由Elsevier出版社在ScienceDirect上出版(http://www.sciencedirect.com/journal/chinese-journal-of-catalysis).